



# Smartphone-powered, ultrasensitive, and selective, portable and stable multi-analyte chemiresistive immunosensing platform with PPY/COOH-MWCNT as bioelectrical transducer: Towards point-of-care TBI diagnosis

Patta Supraja<sup>a</sup>, Suryasnata Tripathy<sup>b</sup>, Shiv Govind Singh<sup>a,\*</sup>

<sup>a</sup> Department of Electrical Engineering, Indian Institute of Technology Hyderabad, 502285, India

<sup>b</sup> Department of Electronics and Communication Engineering, Indian Institute of Information Technology Surat, 395007, India

## ARTICLE INFO

### Keywords:

Point-of-care diagnosis  
Traumatic brain injury  
Smartphone-powered handheld portable electronic readout  
Array of interdigitated microelectrodes  
Chemiresistive immunosensing  
Pyrrole nanocomposite based bioelectrical transducer

## ABSTRACT

Traumatic Brain Injury, one of the significant causes of mortality and morbidity, affects worldwide and continues to be a diagnostic challenge. The most desirable and partially met clinical need is to simultaneously detect the disease-specific-biomarkers in a broad range of readily available body fluids on a single platform with a rapid, low-cost, ultrasensitive and selective device. Towards this, an array of interdigitated microelectrodes was fabricated on commercially existing low-cost single-side copper cladded printed-circuit-board substrate followed by the bioelectrodes preparation through covalent immobilization of brain injury specific biomarkers on carboxylic functionalized multi-walled carbon nanotubes embedded polypyrrole nanocomposite modified interdigitated microelectrodes. Subsequently, the immunological binding events were transduced as the normalized change in bioelectrode resistance with and without the target analyte via current-voltage analysis. As proof of concept, current-voltage responses were primarily recorded using a conventional probe station, and later, a portable handheld-electronic-readout was developed for the point-of-care application. The data compilation and analysis were carried out using the in-house developed android-based mobile app. Notably, the smartphone powered the readout through a PL-2303 serial connector, avoiding integrating power sources with the readout. Further, this technology can be adapted to other point-of-care biosensing applications.

## 1. Introduction

Low-cost, ultra-sensitive and selective quantification of multiple biomarkers simultaneously in easily accessible body fluids (i.e., blood, serum, plasma, urine, tears, etc.) for point-of-care (PoC) diagnostic applications is the most desirable clinical need in recent times. The greatest need for such devices is in diagnosing life-threatening neurological disorders, such as traumatic brain injury (TBI), where every hour delay in treatment increases the mortality and morbidity rate significantly. A detailed explanation of TBI, such as the impact of disease on human health and economy, current diagnostic techniques and their limitations, etcetera, is presented in **Annexure A** of [supplementary material](#). Unfortunately, no single TBI biomarkers (i.e., UCHL1, GFAP, NSE, NfL, S-100 $\beta$ ) have the potential to exhibit appropriate sensitivity and specificity, which plays a crucial role in evaluating the severity of the injury

and patient prognosis at different stages of TBI (i.e., mild, moderate and severe) [1–5]. So, multiplexed detection of multiple biomarkers with ultra-sensitivity and specificity is essential to serve the purpose – our work aimed at this view. Notably, the simultaneous detection of UCHL1 and GFAP in blood or blood-derived products (i.e., plasma/serum) at significantly low concentrations (i.e., sub nano to picogram per mL) was recently approved by the Food and Drug Administration (FDA), having a high potential to detect TBI at various stages [6]. In this view, we reported the design and development of a low-cost, ultra-sensitive and selective, stable and portable multi-analyte sensing platform for simultaneous detection of FDA-approved TBI-specific UCHL1 and GFAP biomarkers in human plasma, specifically toward PoC TBI diagnosis.

Among various transduction mechanisms (i.e., mechanical, optical, thermal, electrochemical and electrical) based biosensors, electrochemical transduction has been highly preferred for PoC applications

\* Corresponding author.

E-mail addresses: [ee17resch01006@iith.ac.in](mailto:ee17resch01006@iith.ac.in) (P. Supraja), [suryasnata@iitisurat.ac.in](mailto:suryasnata@iitisurat.ac.in) (S. Tripathy), [sgsingh@ee.iith.ac.in](mailto:sgsingh@ee.iith.ac.in) (S. Govind Singh).

<https://doi.org/10.1016/j.bioelechem.2023.108391>

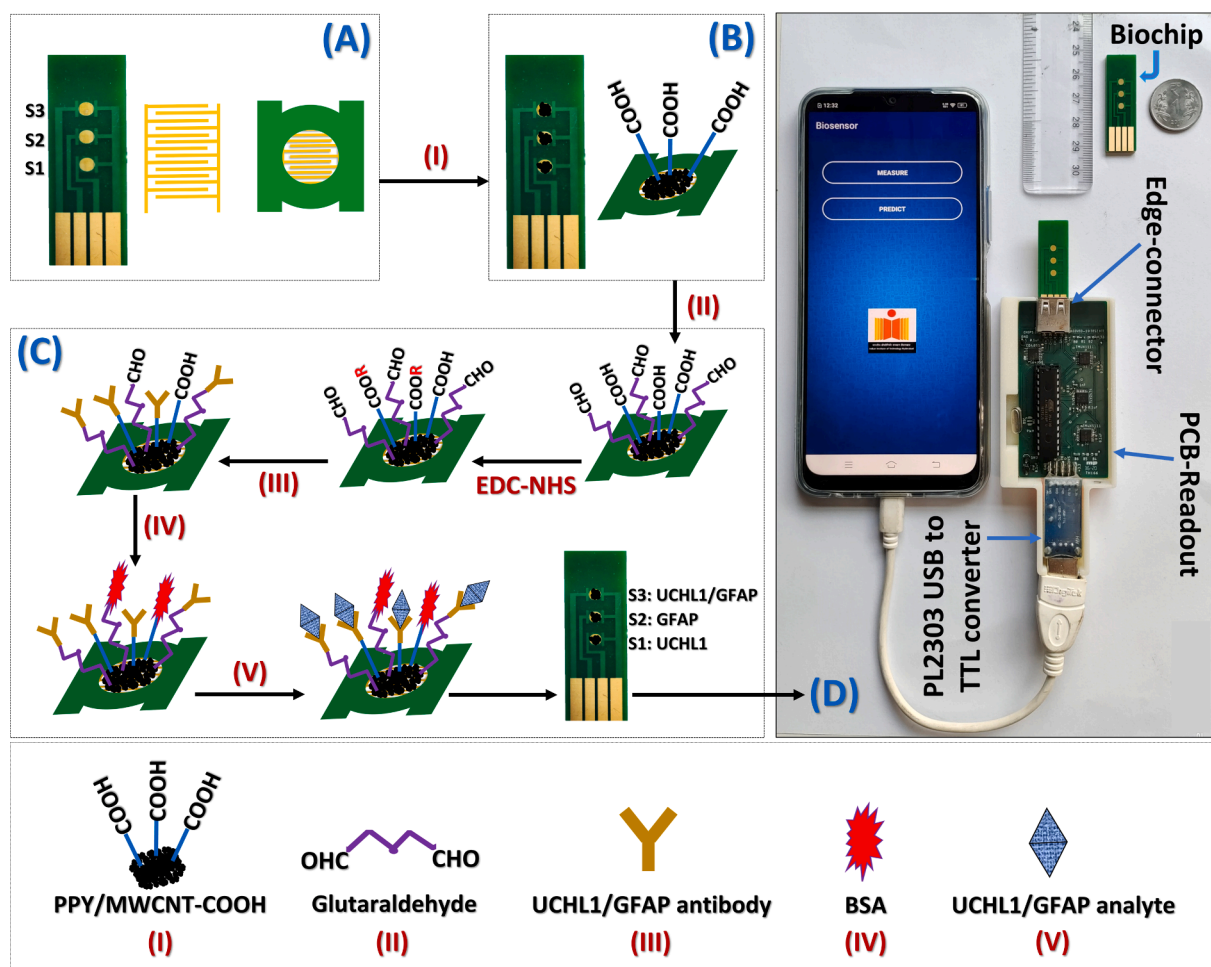
Received 18 October 2022; Received in revised form 24 December 2022; Accepted 27 January 2023

Available online 9 February 2023

1567-5394/© 2023 Elsevier B.V. All rights reserved.

over the past several decades. On the other hand, electrical transduction is one of the viable alternative to electrochemical transduction, which has a high potential to extend to PoC applications due to its cost-effectiveness, ease of fabrication, fast response, amenability towards miniaturization, and minimal or almost no sample preparation [7–9]. Further, the possibility of integration with nanotechnology (i.e., integration with nanomaterials) accounts for its better sensing performance (i.e., sensitivity, limit, and dynamic range of detection). Previously, numerous metal oxides and its composites, conducting polymers, carbon and its derivatives, were used as transducing materials in combination with these platforms [10–14]. Among these, conducting polymers, specifically polypyrrole (PPY), have created substantial research interest because of its ease of synthesis and surface modification, biocompatibility, environmental stability, and feasibility in tuning electrical properties during the synthesis itself. Even though PPY has significant advantages over other polymers, it lacks in terms of long-term stability, which is essential when using it as a bioelectrical transducer. The origin of such instability is eminently due to the performance degradation of nanomaterials in long-term storage [15–18]. So, one must improve the long-term stability of PPY without affecting its other properties. This can be achieved by embedding the secondary phase materials in the primary matrix (i.e., composites) [19–22]. In addition to this, the sensing platform's sensitivity and LoD along with stability can also be improved if the embedded secondary phase material is functionalized and conducting in nature [23–27]. The explanation for the same is elaborated in

**Annexure A of supplementary information.** Given this, we selected carboxylic (–COOH) functionalized multi-walled carbon nanotubes (f-MWCNTs) as a secondary phase material and the corresponding PPY and f-MWCNT nanocomposite (PPY/f-MWCNT) was prepared using chemical-oxidative polymerization method (resulting in high yield and controlled conductivity by tuning monomer and oxidant concentration ratio). Further, as-synthesized nanocomposite was integrated with interdigitated microelectrodes (ID $\mu$ Es) to create an electrical bridge between the electrode's fingers. Furthermore, due to the change in chemical environment (i.e., surface-modification/antibody-immobilization/antigen–antibody immunoreaction), the surface potential of the nanocomposite is altered, thereby changing the electrical properties (i.e., resistance/capacitance/impedance). By correlating this change with the target analyte concentration, one can quantify the desired biomarkers. In our previous work, a similar principle was adapted to detect the UCHL1 and GFAP target analytes in terms of change in capacitance (AC analysis) of PPY/f-MWCNT [28]. Though, the results showed excellent selectivity and sensitivity with LoD in range of fg/mL, adapting the same technology for PoC applications is challenging [28]. As an alternative to this, here we have extended our work in terms of resistance change (DC analysis), which has a high potential to serve as PoC applications by developing handheld portable electronic readout. Specifically, an array of ID $\mu$ Es based multi-analyte sensing platform was utilized to detect UCHL1 and GFAP target analytes simultaneously on the same substrate in terms of variation in the resistance of PPY/f-



**Scheme 1.** PPY/f-MWCNT nanocomposite based portable multi-analyte (UCHL1 and GFAP) chemiresistive immunosensing platform – (A) pictorial representation of fabricated biochip (i.e., array of interdigitated microelectrodes (ID $\mu$ Es), inset showing isolation masked ID $\mu$ Es defining specific circular working area of each sensor), (B) PPY/f-MWCNT nanocomposite modified biochip, (C) protocol for preparation of UCHL1 and/or GFAP bioelectrodes, (D) pictorial representation of handheld-portable electronic readout platform.

MWCNT nanocomposite (i.e., bioelectrical transducer).

The proposed portable multi-analyte chemiresistive immunosensing platform involved four major steps, namely – (1) Low-cost chip with an array of ID $\mu$ Es fabricated on PCB substrate, (2) Synthesis of PPY/f-MWCNT bioelectrical transducing nanocomposite and its incorporation onto the working area of the chip followed by immobilization of bioreceptors, (3) Portable readout circuitry board for electrical measurements, (4) Android-application based mobile interface for data collection and analysis. The schematic of the proposed multi-analyte sensing platform with various preparation steps is presented as [scheme 1](#), and a detailed description of each step is provided in [section 2.2](#). Further, in [table S1 \(Annexure A of supplementary information\)](#), the analytical sensing performance of the proposed platform is weighted against recent literature. As can be seen, the present sensing platform showed superior performance concerning limit of detection and range of detection. Moreover, it also facilitated simultaneous multianalyte detection on the same substrate. Embedding such a feature in sensing systems is essential to enhance the diagnostic accuracy of disease. Further, in terms of the testing cost and time, the developed multi-analyte sensing platform shows a clear advantage over existing single analyte testing platforms. Furthermore, developing a portable handheld readout and its integration with the android mobile interface for data collection and analysis provided the feasibility of adapting the proposed sensing platform for PoC applications.

## 2. Materials and methods

### 2.1. Materials and reagents

N-N-dimethylformamide (DMF), pyrrole, ferric chloride hexahydrate (FeCl<sub>3</sub>·6H<sub>2</sub>O), ethanol, acetone, isopropanol (IPA), phosphate buffered saline (PBS, 0.01 M) tablets, carboxylic functionalized multi-walled carbon nanotubes (3–15 walls, 10  $\mu$ m length), glutaraldehyde (GD), 1-Ethyl-3-(3-dimethyl aminopropyl) carbodiimide (EDC), N-Hydroxy succinimide (NHS), human serum albumin (HSA), bovine serum albumin (BSA), streptavidin (Stpvd), troponin T and I (Tpn-T and Tpn-I) were purchased from Sigma-Aldrich, USA. Ubiquitin carboxy-terminal hydrolase L1 protein (UCHL1, 14–855) and glial fibrillary acidic protein (GFAP, 345996) were purchased from EMD Millipore Corporation, USA. Further, anti-UCHL1-antibody (ab75275), anti-GFAP-antibody (ab10062), human-Tau (Tau, ab246005) and phosphorylated Tau 181 protein (P-Tau, GMP181), amyloid-beta 1–42 peptide (AB42, ab120301), amyloid-beta 1–40 peptide (AB40, ab120479), amylin (A6594) and insulin (I2643) were purchased from Abcam, UK. Deionized water (resistivity 18.4 M $\Omega$ -cm<sup>-1</sup>) from the Q-Millipore water purification system was used for all experimental protocols.

### 2.2. Methods and protocols

#### 2.2.1. Synthesis of PPY/f-MWCNT nanocomposite

In this work, f-MWCNTs embedded PPY nanocomposite was prepared using the protocol mentioned in our earlier publication [28]. In brief, pyrrole, ferric chloride, and MWCNTs were utilized as a monomer, oxidizing agent, and conductive fillers, respectively. Initially, 0.05 M of pyrrole prepared in DI water was added dropwise to 0.1 M of ferric chloride solutions under vigorous stirring for 20 min to initiate the polymerization reaction. To this mixture, 0.1 % (w/v) f-MWCNTs was added and allowed to stir for a minimum of 4 h, resulting in a black precipitate. The resulted precipitate mixture was filtered and washed several times with DI water, acetone and ethanol consecutively. Such a multi-stage washing step is essential to remove the reaction byproducts from the filtered product. Finally, the washed black residue was air-dried overnight at 60 °C in an incubator. At last, the dried powder was collected in an air-tight glass vial and stored at room temperature whenever not in use. The same procedure was followed to synthesize various PPY/f-MWCNT nanocomposites (PMC\_0.2 % and PMC\_0.3 %) by

varying the weight percentages of f-MWCNTs (0.2 % and 0.3 %), respectively. The pristine PPY was synthesized following the procedure mentioned above without adding f-MWCNTs, and was utilized for comparison purposes.

#### 2.2.2. Preparation of bioelectrode

Bioelectrodes for detecting TBI-specific UCHL1 and GFAP biomarkers were prepared through covalent immobilization of anti-UCHL1 and anti-GFAP antibodies onto the working area of ID $\mu$ Es (inset of [Scheme 1\(A\)](#)). The array of ID $\mu$ Es (i.e., biochip) fabricated on commercially existing cost-effective printed circuit board (PCB) substrate having single-sided copper clads is already mentioned in our previous publication [28]. A detailed description of biochip dimensions and ID $\mu$ Es feature size is provided in [Annexure A of supplementary material](#). The bioelectrode preparation ([Scheme 1\(B\) and 1\(C\)](#)) was carried out in four steps, namely – (1) nanomaterial modification, (2) surface functionalization, (3) antibody immobilization, and (4) non-specific binding site blocking. Initially, 1.5  $\mu$ L of PPY/f-MWCNT (1 mg/mL in DMF) nanocomposite dispersion was drop-casted onto each working area of ID $\mu$ Es (i.e., S1, S2 and S3), followed by air-drying at 60 °C for 20 min in the incubator. Subsequently, to create aldehyde (–CHO) functional groups on PPY nanoparticles present in PPY/f-MWCNT nanocomposite, the modified ID $\mu$ Es were incubated with 2.5 % GD solution (Bifunctional linker, 1.5  $\mu$ L) for 15 h. To activate the carboxylic (–COOH) functional groups present on the f-MWCNTs, these electrodes were further incubated with 1.5  $\mu$ L of 0.4 M EDC and 0.1 M NHS mixture for 4 h at room temperature. Such activation converts the –COOH groups to an ester (–COOR), known as esterification. Later, 1.5  $\mu$ L of antibody solution (UCHL1 and/or GFAP) was drop-casted onto each surface-functionalized PPY/f-MWCNT electrodes (i.e., GD treated followed by EDC-NHS activated) and incubated at 4 °C for 12 h. During the incubation, the amine (–NH<sub>2</sub>) end of the antibody interacts with the ester (–COOR) and aldehyde (–CHO) groups that are present on the surface-activated electrodes and form a covalent amide (CO–NH) and imide (C=N) bond, respectively. Subsequently, to block the unbonded binding sites on the electrode surface, 1.5  $\mu$ L of BSA solution was drop-casted onto the electrodes' working area and incubated at 37 °C for 30 min. Post-incubation, the electrodes were washed with PBS and dried at room temperature. When not in use, the as-washed and dried electrodes were packed in sealed air-tight boxes and stored at 4 °C. **Note:** S1 and S2 sensors are dedicated to UCHL1 and GFAP, respectively, whereas, in S3, one can use either UCHL1 or GFAP based on the requirement.

#### 2.2.3. Development of portable readout platform

In this work, towards the point-of-care diagnosis of TBI, a portable handheld PCB-based electronic readout was designed and developed to measure the sensors' electrical DC resistance. A pictorial representation of the same is shown in [Scheme 1\(D\)](#). As shown, the electronic readout majorly contains five parts, namely – (1) female edge connector: to connect the biochip to the readout board, (2) PL-2303 serial connector: to interface the readout with an android-application based smartphone and also to powerup the readout from mobile, (3) multiplexing circuit: to switch between three sensors present on the biochip during resistance analysis, (4) microcontroller: to carry the operational logic (i.e., multiplexer switching, reference resistance estimation using SARS algorithm [29,30], voltage divider logic to calculate the sensor resistance based on estimated reference resistance), and (5) voltage divider circuit using operational amplifiers. Along with this readout, an android-based application was developed to facilitate data acquisition from the portable readout. The said application offers a simple user interface (UI) and accounts for a minimally interacting protocol for the desired data acquisition. Protocol for data acquisition from the readout using an android application-based mobile interface and consolidated mobile screenshots of the same protocol at every step are provided in [Annexure B of supplementary information](#).

### 2.2.4. Protocols for target analytes preparation and detection

**Target analyte preparation** – In this work, all the initial stock solutions of all target analytes (i.e., UCHL1 and GFAP) were prepared in the buffer solutions (as specified in the products' datasheet), and the corresponding lower concentrations in the matrix (i.e., plasma) were prepared through the serial dilution protocol. Further, the initial stock solutions of the analytes were stored at  $-20\text{ }^{\circ}\text{C}$ , and the corresponding serial-diluted low-concentrated samples were held at  $4\text{ }^{\circ}\text{C}$  whenever not in use. Notably, in this work, a pooled human plasma obtained from the ESIC hospital laboratory (Employees State Insurance Corporation: Hyderabad, India) was used for real-time-plasma based detection studies.

**Target analyte detection** - In this work, towards label-free detection of the target analytes through chemiresistive transduction mechanism, a  $1.5\text{ }\mu\text{L}$  of TBI-specific target analyte (UCHL1/GFAP) spiked in human plasma was added onto each working area of bioelectrode and allowed to incubate at  $37\text{ }^{\circ}\text{C}$  for 30 min, to facilitate the specific antigen and antibody interaction. Post incubation, the bioelectrodes were washed with PBS buffer following the washing protocol mentioned in **Annexure B** of [supplementary information](#). Such a washing step ensures the removal of non-specifically adsorbed analytes from the bioelectrode surface before recording their electrical response (i.e., probe station/portable readout).

**Electrical current-voltage (I-V) measurement** – The DC Electrical I-V (i.e., Resistance) measurements reported in this work were carried

out in two ways – (1) conventional cascade summit 11 K probe station (two-probe arrangement) combined with Agilent B1500A parametric analyzer, (2) handheld portable PCB based readout interfaced with an android application-based smartphone. In the conventional probe station, initially, the electrical contact between two ID $\mu$ Es was established by probing the metallic tips of precision positioners. Later, a specific DC voltage sweep between 0.1 V and 1 V (step size 10 mV) was applied across the device and the corresponding current response was recorded using the parametric analyzer. Subsequently, the device resistance from these recorded I-V responses was calculated using the ohms law. A schematic of the probe-station setup used for I-V characterization is presented in **Annexure B** of [supplementary information](#) ([fig. S3](#)). On the other hand, in the case of portable readout, initially, the electrical contact between contact pads of ID $\mu$ Es and edge connector pins was established by inserting a biochip into the female connector. Later, the chemi-resistance of each sensor on the biochip was measured by switching the multiplexing circuit digitally among the three sensors. The same data was displayed on the mobile screen using an android application-based user interface. A detailed description of the protocol for data acquisition from the readout using an android application-based mobile interface and consolidated mobile screenshots of the same at every step are provided in **Annexure B** of [supplementary information](#).

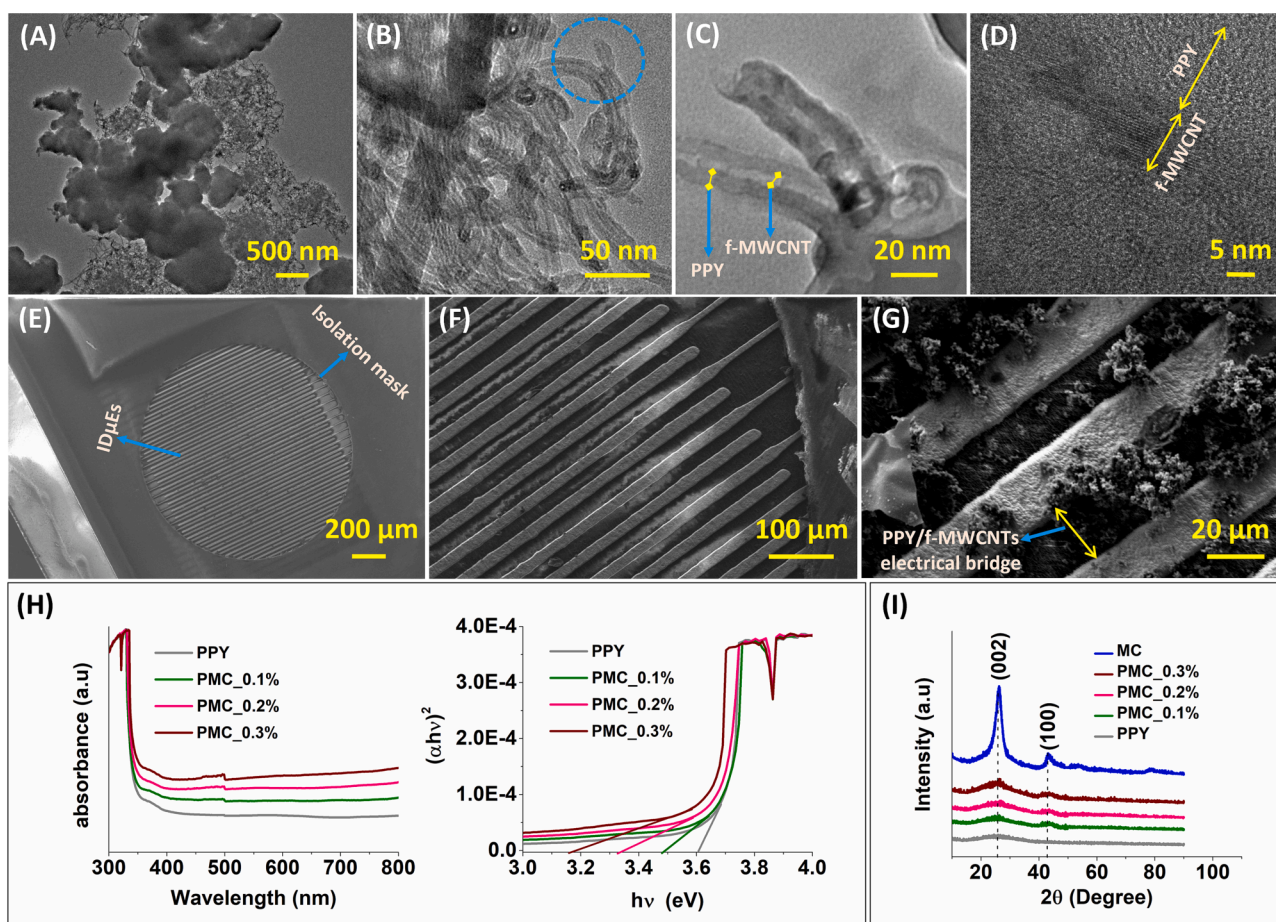


**Fig. 1.** Characterization: (A)-(C) TEM image of PPY/f-MWCNT nanocomposite at various magnifications, (D) HRTEM image depicting the crystallinity nature of MWCNTs, amorphous nature of PPY and interface of both, (E) SEM image of ID $\mu$ Es with 2.4 mm diameter circular isolation mask, (F) magnified image of [Fig. 1 \(E\)](#) depicting 25  $\mu\text{m}$  finger width and 30  $\mu\text{m}$  inter-finger distance, (G) SEM image of nanocomposite modified ID $\mu$ Es forming the electrical bridge between two successive fingers of electrodes, (H) UV-VIS absorbance spectroscopic and corresponding Tauc plot based bandgap analysis of PPY/f-MWCNT nanocomposites by varying f-MWCNTs weight percentage as 0 (PPY), 0.1 (PMC\_0.1 %), 0.2 (PMC\_0.2 %) and 0.3 (PMC\_0.3 %), respectively, (I) XRD analysis of pristine PPY, MWCNT and its nanocomposites.

### 3. Results and discussion

#### 3.1. Characterization of PPY/f-MWCNT nanocomposites and ID $\mu$ Es

The structural and morphological analysis of the PPY/f-MWCNTs nanocomposite was carried out using Transmission Electron Microscopy (TEM, JEOL 2100), and the corresponding images at various resolutions are presented in Fig. 1(A)–2(D). Initial, Fig. 1(A) and 2(B) depict the networking structure of nanocomposite at various magnifications after drop-casting onto a copper grid. Further, Fig. 1(C) (magnified version of Fig. 1(B) at specified region) discloses the coaxial morphology of nanocomposite, in which long MWCNTs were uniformly encapsulated by PPY nanoparticles coating. Furthermore, high-resolution TEM (HRTEM) shown in Fig. 1(D) depicted the amorphous and crystalline nature of PPY and MWCNTs (0.33 nm interlayer spacing), respectively. The close interfacial contact between PPY and f-MWCNT validated the successful synthesis of PPY/f-MWCNT nanocomposite. Fig. 1(E) and 1(F) represent the Scanning Electron Microscopic images of ID $\mu$ Es (i.e., fabricated on PCB substrate) at various magnifications, depicting the width of 25  $\mu$ m and inter-finger distance of 30  $\mu$ m. Fig. 1(E) also shows 2.4 mm diameter circular isolation mask on top of ID $\mu$ Es, which is the uniform working area of each device. In addition to this, it also prevents the mixing of liquid between two adjacent devices on the biochip. Further, Fig. 1(G) shows the SEM image of nanocomposite drop casted ID $\mu$ Es, which shows the aggregation of nanocomposite between two successive neighbouring fingers of ID $\mu$ Es, resulting in a conducting pathway between the electrodes (i.e., electrical bridge).

Further, the optical bandgap analysis of these nanocomposites was carried out using UV-Visible spectroscopy (UV-VIS, PerkinElmer Lambda 750). Fig. 1(H) represents the absorption spectrum with corresponding Tauc plots of 0.1 %, 0.2 % and 0.3 % f-MWCNTs embedded PPY nanocomposites (PMC\_0.1 %, PMC\_0.2 % and PMC\_0.3 %) in comparison with pristine PPY. As can be seen, the pristine PPY absorption band was observed at 341 nm, whereas it shifted to 355, 371 and 394 nm when embedded with various weight percentages of MWCNTs (0.1 %, 0.2 %, and 0.3 %). Such increment in absorption wavelengths to higher values can be attributed to the band gap reduction of nanocomposite ( $E_g = hc/\lambda$ ), calculated by the Tauc relation ( $(\alpha h\nu)^2 = h\nu - E_g$ ). In graphical view, the x-intercept of the Tauc plot ( $(\alpha h\nu)^2$  vs  $h\nu$ ) indirectly depicts the material's bandgap. The detailed discussion of the same is provided in Annexure B of supplementary information. By using the Tauc relation and corresponding plot, we found the bandgap of PPY, PMC\_0.1 %, PMC\_0.2 % and PMC\_0.3 % as 3.64, 3.49, 3.33 and 3.15 eV,

respectively. Furthermore, crystallographic analysis of the same nanocomposites was carried out using X-ray diffraction spectroscopy (XRD, Bruker Cu K $\alpha$  Radiation,  $\lambda = 1.54 \text{ \AA}$ ) and as-recorded diffraction spectrums in comparison with pristine f-MWCNTs and PPY is presented in Fig. 1(I). As can be seen, two sharp peaks at 25.8° and 43.4° correspond to pristine MWCNTs (MC) i.e. diffractions of graphite C(002) and C(100) planes, respectively [31–33]. Further, the broad peak at 25.3° corresponds to pure PPY i.e. intermolecular spacing of pyrrole [34–36]. Moreover, the composites of PPY and f-MWCNTs showed both PPY broad peak (25.3°) and MWCNTs peaks (25.8° and 43.4°), confirming the successful synthesis of the nanocomposite without losing its nature of crystallinity. Further, it was also observed that the diffraction peak intensity of MWCNTs increased with increasing the weight percentage of MWCNTs embedded into the PPY matrix (0.1 % to 0.3 %), notably, all stronger than PPY intensity. The peak positions detected correlate well with the literature [37–40], hence confirming the successful synthesis of PPY/f-MWCNT nanocomposite.

#### 3.2. DC electrical characterization of PPY/f-MWCNT nanocomposites

Embedding MWCNTs into the PPY as secondary phase conducting

fillers improves the conductivity of PPY. Such a rate of improvement inherently depends on the embedding quantity of MWCNTs. A detailed explanation about origin of such inherent behaviour is presented in section 5 of Annexure A (supplementary information). Notably, in electrical transducers-based biosensors, the sensing platform's sensitivity/resolution in detecting target analytes depends on the electrical conductivity of transducing material. Specifically, too high and too low conductivity is not preferred on account of the poor resolution of the sensor. In view of this, optimizing the weight percentage of f-MWCNTs in PPY/f-MWCNTs nanocomposite is crucial. Fig. 2(A) depicts the I-V responses of PPY/f-MWCNT nanocomposite modified ID $\mu$ Es (PMC\_0.1 %, PMC\_0.2 % and PMC\_0.3 %) recorded using conventional I-V probe station in combination with Agilent B1500A semiconductor parametric analyzer in the voltage range of –1 to +1 V (experimental setup shown in Annexure B of supplementary information). Further, Fig. 2(B) demonstrates the comparative list of current responses and corresponding resistances calculated at 0.5 V of each I-V curve shown in 3(A). As can be seen, increasing the weight percentages of embedded f-MWCNTs from 0.1 % to 0.3 % increased the current response and reduced resistance. More, the same trend is persisted even for various solution concentrations of composites (1 mg/mL and 2 mg/mL). Specifically, resistances of all PMC nanocomposites are lower than the bare PPY, indicating the successful embedding of MWCNTs into PPY to improve the conductivity. Also, except for PMC\_0.1 % (1 mg/mL), all other PMC resistances are below 1 K $\Omega$ . Since highly conducting nanomaterials are not preferred for biosensors as bioelectrical transducers, 1 mg/mL concentrated PMC\_0.1 % was selected as optimized material for sensor design.

#### 3.3. Analysis of matrix effect

As mentioned in the introduction, according to FDA, detecting UCHL1 and GFAP target analytes in blood or its derived products such as plasma and/or serum have the high potential to diagnose TBI accurately at various stages. Blood is a complex liquid containing several cells (Red and white blood cells), proteins, peptides and ions. These can non-specifically interact with bioelectrode and produce a significant unwanted response that inherently deteriorates the sensing platform's LoD, known as the matrix effect. On account of reducing the matrix effect, we moved towards blood-derived plasma/serum products where red and white blood cells can be separated effectively. Further, plasma is preferred between plasma and serum because of its high sample yield, no delayed clotting and less risk of hemolysis during separation. Additionally, on-chip separation of plasma over serum is facile and less complex, which is essential for PoC applications. Notably, in this work, a microfluidics-based on-chip portable system designed and developed by our research group was used to separate plasma from the blood [41]. Even though plasma shows less interference than blood, it still offers a significant response due to various common proteins, peptides and enzymes. So, one must reduce the matrix effect further. Dilution of plasma with buffer is one of the strategic ways to reduce the matrix effect effectively. In view of this, we have diluted 100 % human plasma with PBS buffer at various percentages (50 %, 25 %, 10 % and 5 %), and the electrical I-V responses of UCHL1 and GFAP bioelectrodes to these undiluted and diluted samples were recorded separately to determine the baselines against blank samples in terms of normalized change in the electrical resistance of bioelectrode ( $\Delta R/R_0$ ,  $R_0$  is absolute resistance of bioelectrode and  $\Delta R$  is the resistance variation of bioelectrode after incubating with various target samples). As recorded, normalized resistances of bioelectrodes against plasma and PBS buffer samples are presented in Fig. 2(C). From this fig., it was observed that the normalized change in resistance of UCHL1(GFAP) bioelectrodes to 100 % plasma and 0 % plasma (i.e., PBS buffer) is 6.8 (8.5) and 0.5 (0.3), respectively. Further, the response of bioelectrodes decreased with an increase in the dilution of plasma, indicating a lowering of the matrix effect. Notably, the 5 % plasma sample response is identical to the PBS

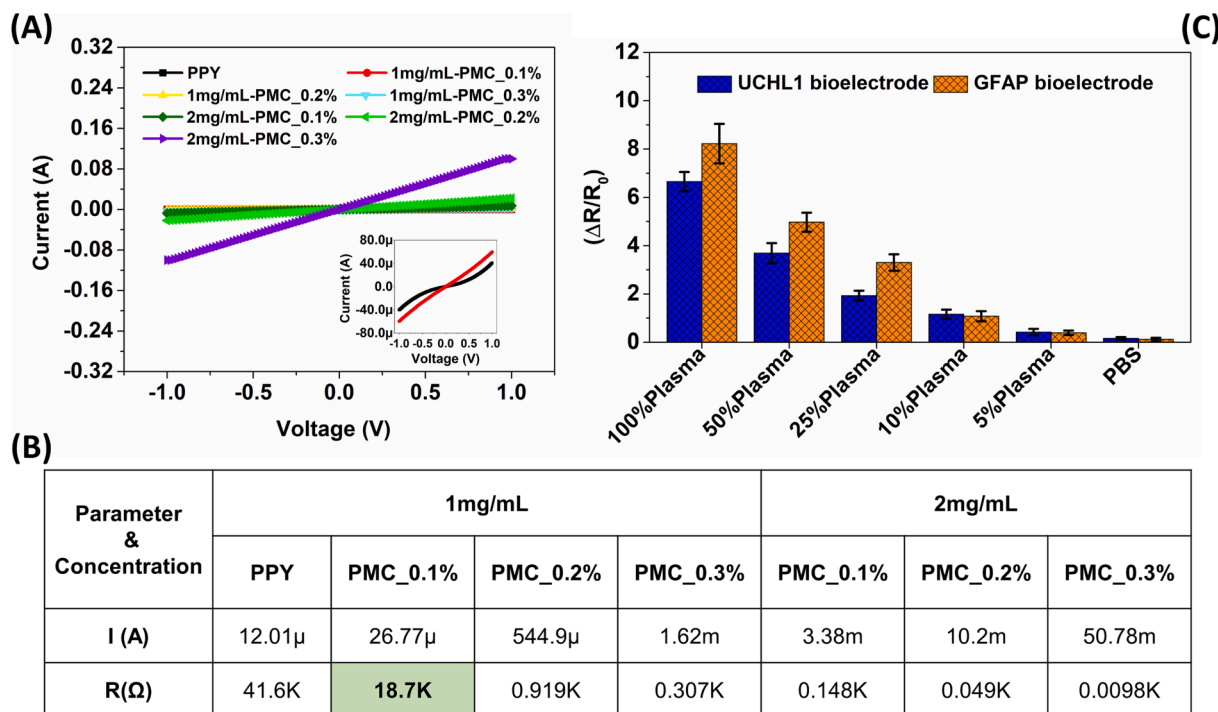


**Fig. 2.** (A) I-V characterization (DC analysis, -1 to 1 V) of IDμEs modified with 1 and 2 mg/mL concentrations of nanocomposites (PMC\_0.1 %, PMC\_0.2 % and PMC\_0.3 %), inset showing the I-V responses of 1 mg/mL of PPY and PMC\_0.1 on the magnified scale, (B) DC electrical resistance (i.e., output current at 0.5 V input) comparison of PPY and its nanocomposites, (C) Plasma optimization: normalized change in resistance ( $\Delta R/R_0$ ; where  $R_0$  is the resistance of the bioelectrode) of PMC\_0.1 % nanocomposite based UCHL1 and GFAP bioelectrodes to blank PBS and plasma (100 %, 50 %, 25 %, 10 % and 5 %) (n = 3).

response, representing a minimal matrix effect. In lieu of this, all the UCHL1 and GFAP target analyte doses were prepared in 5 % real-time human plasma samples for envisaged TBI diagnosis. Note: The absolute values of the histograms shown in Fig. 2(C) are presented in table S2 of supplementary information.

3.4. Detection of UCHL1 and GFAP target analytes

Towards target analyte detection, the UCHL1 and GFAP antibody immobilized bioelectrodes (i.e., biochip) were exposed to various concentrations of target analytes (10 fg/mL-1 μg/mL, spiked in 5 % human plasma), corresponding I-V responses were recorded and the same are

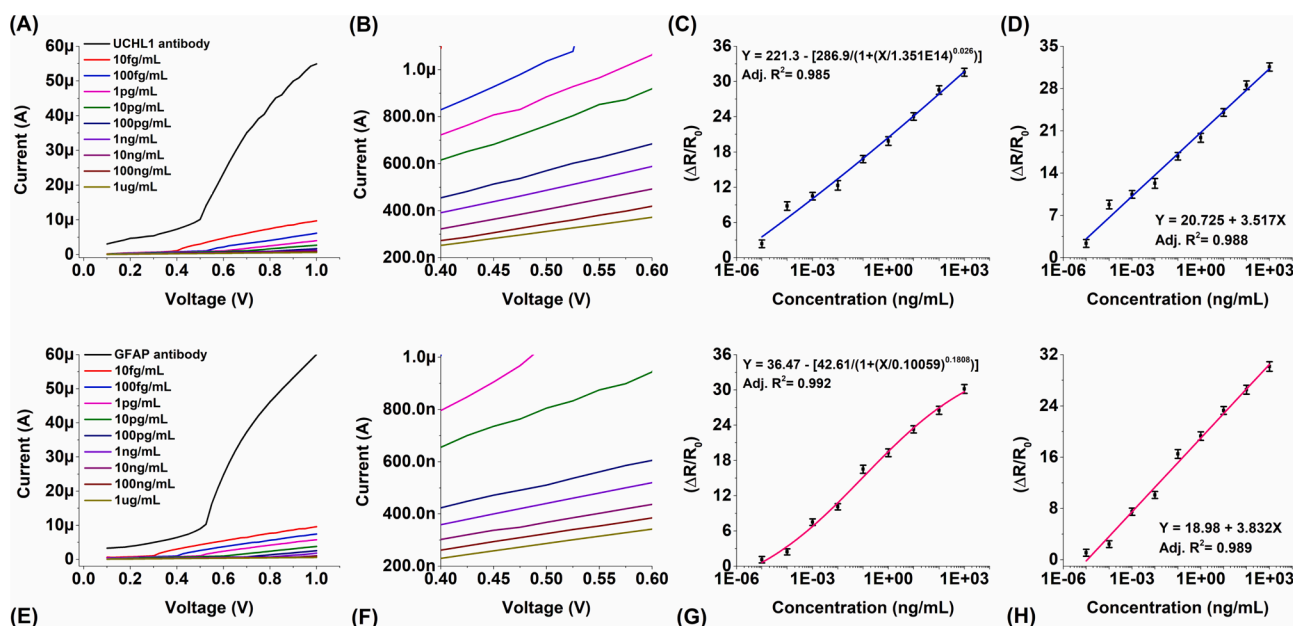


**Fig. 3.** (A) and (E) electrical I-V responses of PMC\_0.1 % nanocomposite-based anti-UCHL1 and anti-GFAP antibody immobilized bioelectrodes for 10 fg/mL–1 μg/mL concentrations of UCHL1 and GFAP target analyte spiked 5 % plasma samples, respectively. (B) and (F) magnified version of I-V responses shown in Fig. 3. (A) and (E) in 0.4–0.6 V voltage range, respectively. (C) and (G) four-parameter logistic sigmoidal curve fitting for the dose–response characteristics obtained from Fig. 3 (A) and (E), (n = 3), respectively. (D) and (H) linear curve fitting (10 fg/mL–1 μg/mL) for the dose–response characteristics obtained from Fig. 3(A) and (E), (n = 3), respectively.

shown in Fig. 3(A) and 4(E), respectively. As can be seen, in the wide range (0.1 to 1 V), the responses are non-linear, limiting the application of ohm's law for device resistance calculation. So, one can approximate the I-V response to several small segments where piece-wise linearity can be existed and can directly apply ohm's law to calculate the device resistance in the specified range. From Fig. 3(B) and 4(F) (i.e., magnified responses of I-V curves shown in Fig. 3(A) and 4(E) in the voltage range 0.4 to 0.6 V), one can observe that majority of the I-V curves are linear in the specified range. So, the resistive response of I-V curves in the specified range is equal to the average resistance calculated at multiple voltages in the range, which is also equal to the resistance at average voltage (i.e., 0.5 V: average of 0.4 and 0.6 V). Notably, all the resistances shown in this work were obtained with the current response at 0.5 V. Further, from Fig. 3(B) and 4(F), we observed that current response decreased with the increase in target analyte concentration, which can be attributed to the fact that the carrier mobility in PPY/f-MWCNT nanocomposite would with target analyte binding to its corresponding specific antibody (covalently immobilized on the surface of nanocomposite). Such behavior is known as chemiresistive with PPY/f-MWCNT nanocomposite as a chemiresistor (i.e., change in resistance of nanocomposite as a response to change in nearby chemical environment) and specific antibody-antigen interaction on the nanocomposite surface as required stimulation (i.e., chemical interaction). The strength of such stimulative antibody-antigen immuno reaction inherently depends on the binding kinetics of solvent phase antigen (here plasma) and surface-immobilized antibodies. In particular, the binding kinetics depends on various factors, namely – (1) antibody orientation and surface density, (2) concentration of antigen in solution, (3) association and dissociation constants of immunoreaction (i.e., antibody-antigen binding). On account of these, the binding fraction varies directly in accordance with the change in target analyte concentration near the sensor surface, and therefore, the incremental change in device resistance was observed with respect to target analyte concentrations. In addition to the factors mentioned above, the binding kinetics also get affected by mass transport of target analytes in solution phase (i.e., diffusion rate). Specifically, small target diffusion lengths are preferred for faster kinetics. One can modulate the diffusion length by controlling the test sample's volume near the sensor surface. In view of this, a solder mask with specific openings was used to define circular working areas on the.

ID $\mu$ Es, which can hold a maximum of 2  $\mu$ L sample volume without spilling it out of the device working area. Notably, in this work, the bioelectrodes were incubated with 1.5  $\mu$ L of the target UCHL1 and GFAP. Since the sample volume is minimal (shorter diffusion length), the binding kinetics is not limited by mass transport, resulting in enhanced interaction of antibody and antigen, which can be transduced in terms of variation in bioelectrode resistance before and after the addition of specific target analyte concentrated test sample. In view of this, the proposed testing protocol is advantageous. Further, Fig. 3(C-3(D) and 3(G)-3(H) show the dose–response characteristics of UCHL1 and GFAP bioelectrodes for 10 fg/mL–1  $\mu$ g/mL concentrations of UCHL1 and GFAP target analytes spiked in 5 % plasma. To derive the empirical correlation between the normalized change in resistances of bioelectrodes ( $\Delta R/R_0$ ) for the various target analyte concentrations, the dose–response characteristics were fitted with a logistic sigmoidal model resulting in calibrated equations (with a correlation coefficient of 0.985 and 0.992), appended in corresponding figures. Further, the accuracy of calibrated equations in determining the target analyte concentration in the test sample is investigated by comparing the target dose (T) with estimated dose (E). For this, the prepared bioelectrode's response to several target samples is recorded, and the estimated dosage was back calculated using the obtained calibration equations. As calculated doses were compared with the target dose in table S3. From the error values of the dose prediction from the response (error column in table S3), one can conclude that the proposed immunosensing platform can detect both the UCHL1 and GFAP analytes effectively in human plasma with reasonably good accuracy in the 10 fg/mL–1  $\mu$ g/mL range. Further, the proposed

PPY/f-MWCNT based sensing platforms' sensitivity and theoretical LoD was computed using the standard procedure presented in Annexure C of supplementary information [42]. The sensitivity and LoD were calculated as 77.75 ( $(\Delta R/R_0)/\text{ng.mL}^{-1}$ )/ $\text{cm}^2$  and 0.197 fg/mL, respectively for UCHL1, and 84.70 ( $(\Delta R/R_0)/\text{ng.mL}^{-1}$ )/ $\text{cm}^2$  and 0.181 fg/mL, respectively, for GFAP. In view of medically relevant plasma levels of UCHL1 and GFAP peptides in diagnosing TBI, these LoDs are considerable, thus, making the proposed biosensing platform suitable for the targeted diagnosis of mild TBI along with moderate and severe.

In addition to detecting TBI-specific biomarkers through conventional probe station based I-V characterization, the response of UCHL1 and GFAP bioelectrodes for various concentrations of specific target analyte samples was also recorded using the portable PCB readout (shown in Scheme 1(D)) through interfacing it with android application based mobile. As-recorded normalized responses ( $\Delta R/R_0$ ) of sensors (UCHL1 and GFAP) were compared with the responses of sensors measured with probe-station setup (bulky and costly), and the comparative study is presented in Fig. 4. As can be seen, the low-cost and portable PCB readout produced more or less same response with marginal deviation (assigned to the associated electronics). This demonstrated that the proposed PPY/f-MWCNT nanocomposite based multi-analyte sensing platform combined with the portable PCB electronic readout and the android application is appropriate for PoC diagnosis of TBI.

### 3.5. Stability, selectivity, interference repeatability, and reproducibility analysis

Testing sensing platform's efficiency in terms of long-term stability, repeatability, reproducibility, selectivity and interference with most abundantly existing non-specific targets is essential before adapting it for real-time PoC applications. A detailed description of testing protocols and obtained results is presented below categorically.

**Stability** – To evaluate the degradation performance of PMC 0.1 % nanocomposite based UCHL1 and GFAP bioelectrodes with time, corresponding responses of the bioelectrodes stored at 4 °C in sealed airtight package were recorded after 30 weeks of storage. During this storage time, the absolute resistance of UCHL1 and GFAP bioelectrodes ( $R_0$ ) varied by 17.1 % ( $n = 3$ ) and 14.69 % ( $n = 3$ ) compared to day0, respectively. Also, in regard with shelf life, the bioelectrode's  $R_0$  was measured after every three weeks for 30 weeks: as-measured data in terms of change in resistance with respect to day0 (i.e.,  $\Delta R/R_0$ ) is represented in Fig. 5(A). As can be seen, within 30 weeks of storage,  $R_0$  of UCHL1 and GFAP bioelectrodes varied by 18.45 % and 17.03 % compared to day0, which is significantly less compared to the variation of PPY-based UCHL1 and GFAP bioelectrodes (i.e., 75 % and 69 %), indicating excellent long-term stability.

Further, in order to confirm such improvement in the stability of bioelectrodes is due to the introduction of a secondary phase into the PPY nanomaterial (i.e., nanocomposite), one has to investigate the long-term stability of nanocomposite with respect to time. In view of this, the pure PPY and PPY/f-MWCNT nanocomposite modified ID $\mu$ Es were stored for 30 weeks, and the corresponding responses (i.e., resistance) were recorded periodically every three weeks once. As-recorded data in terms of change in resistance with respect to day0 (i.e.,  $\Delta R/R_0$ ,  $R_0$ –resistance of nanomaterial at day0) is represented in Fig. 5(B). The results showed that within thirty weeks of storage, the resistance of PPY varied by 115.9 %, whereas the same for PPY/f-MWCNT nanocomposite varied by 47.51 %. This confirmed that adding MWCNTs to PPY as a secondary phase significantly improved the nanomaterial's stability, inherently assisting in enhancing the sensing platform's overall stability.

**Selectivity and Interference** – The selectivity and interference analysis of the proposed platform was carried out against several non-specific proteins related to Alzheimer's (AB40, AB42, Tau, P-Tau), cardiac arrest (Tpn-I, Tpn-T), diabetes (Amylin, Insulin), and other interfering proteins (BSA, HSA, Stpvd), following the testing protocol

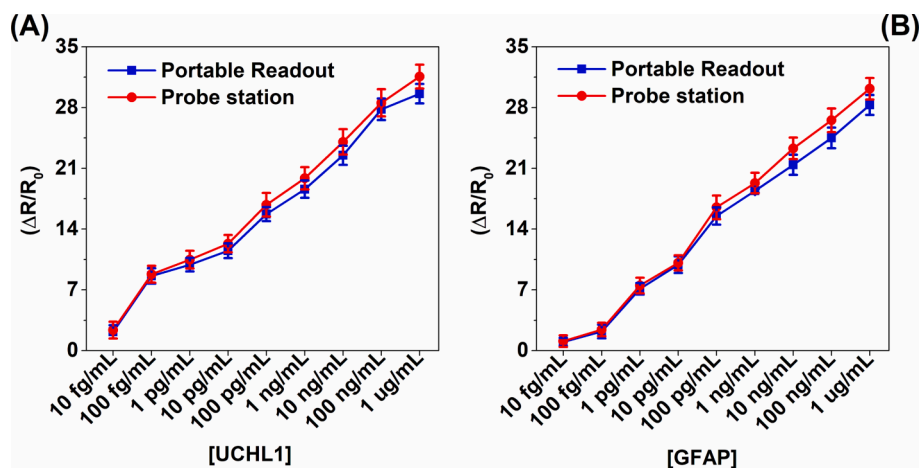


Fig. 4. Comparative study of PMC<sub>0.1</sub> % nanocomposite-based (A) UCHL1 (B) GFAP immunosensor's data ( $\Delta R/R_0$ ) measured with the standard probe-station and portable PCB-based electronic readout ( $n = 3$ ) for 10 fg/mL-1  $\mu$ g/mL (UCHL1/GFAP) concentrations of specific target analytes spiked in 5 % plasma.

mentioned in section 2.2.4. The physical existence of these compounds with their respective concentrations in human plasma is presented in Annexure C of supplementary information. Fig. 5(C) shows the normalized change in resistance of UCHL1 and GFAP bioelectrodes ( $\Delta R/R_0$ ) for each of 10 ng/mL concentrated non-specific compounds mentioned above, in comparison with the same concentration of specific-target analytes (i.e., UCHL1 or GFAP), respectively. As can be seen, compared to the analogous normalized response of bioelectrodes (UCHL1 and GFAP) to the corresponding specific-target analytes ( $\Delta R/R_0$ : UCHL1: 24.043, GFAP: 23.297), the non-specific target analytes response (UCHL1 bioelectrode: 0.2783, 0.223, 0.189, 0.161, 0.099, 0.147, 0.0763, 0.1494, 0.156, 0.091, 0.0825 and 0.28) (GFAP bioelectrode: 0.186, 0.1688, 0.151, 0.148, 0.133, 0.183, 0.095, 0.171, 0.091, 0.107, 0.134 and 0.2098) is significantly low, thus, validating the platform's excellent selectivity towards specific target analytes (UCHL1 or GFAP). Further, towards interference study, the response of both UCHL1 and GFAP bioelectrodes to the mixture of above-mentioned compounds (specific + non-specific) was recorded, and the corresponding normalized change in resistance was calculated as 22.441 and 20.895, respectively. In comparison to the response of bioelectrodes to only specific-target analytes (i.e.,  $\Delta R/R_0$  - UCHL1: 24.043 and GFAP: 23.297), these are almost the same. From this, one can infer that the sensor's response to a specific target analyte with or without the presence of non-specific compounds are nearly the same. This confirmed that the developed immunosensing platform is less prone to interference even in human plasma samples.

**Reproducibility and Repeatability** – Fig. 5(D) represents the reproducibility of the PMC<sub>0.1</sub> % nanocomposite-based protocol, analyzed by measuring the absolute resistance of thirty bioelectrodes ( $n = 30$ ). In addition to this, the repeatability of these bioelectrodes were recorded by taking four consecutive readings, and the corresponding relative standard deviation ( $n = 4$ ) is represented as an error bar at each electrode data point in Fig. 5(D). The maximum %RSD observed for the resistance values recorded against a single bioelectrode (i.e., repeatability) is 2.1 % and 2.5 %, for UCHL1 and GFAP, respectively. Further, the %RSD of the resistance values of thirty distinct UCHL1 and GFAP bioelectrodes (i.e., reproducibility) is 6.91 % and 8.89 %, respectively. These results revealed that the majority of the bioelectrodes followed a certain resistance range with a nominal deviation from the mean, inherently assisting in developing an accurate system to estimate the target analytes concentrations effectively from patient's blind samples.

#### 4. Conclusion

In this work, we developed a low-cost, ultrasensitive and selective,

stable and portable, self-powered immunosensing platform that can detect the FDA-approved TBI-specific plasma UCHL1 and GFAP biomarkers simultaneously on a single platform, intended for the PoC diagnosis of TBI. In order to reduce the production cost of electrodes, lithographic patterned Cu electrodes were electroplated with Ni followed by Au metal through low-cost electrodeposition setup. This inherently aided in reducing the cost per chip significantly. The antibody-antigen binding event occurring on the bioelectrode surface was transduced in terms of variation in DC electrical resistance of the bioelectrical transducer (PPY/f-MWCNT). Further, a portable PCB electronic readout in combination with an android based mobile interface was used for resistive data collection and analysis from multiple sensors on the biochip. Specifically, a multiplexing circuit was explicitly used to switch the operation logic among the three sensors after mounting the biochip onto the PCB readout. Since the portable readout can be powered from a smartphone through a PL-2303 serial connector, one can avoid integrating power sources onto the test kit. This inherently aids in improving portability and reducing the overall cost of the system.

The developed PPY/f-MWCNT based portable immunosensing platform showed sensitivity and LoD as 77.75 (84.7) ( $(\Delta R/R_0)/\text{ng}\cdot\text{mL}^{-1}$ )/ $\text{cm}^2$  and 0.197 (0.181) fg/mL in detecting UCHL1 (GFAP) target analytes in 5 % human plasma samples, respectively. Moreover, the sensing platform's efficiency was evaluated by analysing long-term stability (i.e., 30 weeks of storage), selectivity, interference, repeatability, and reproducibility. Notably, the said portable PCB readout reproduced the data of the conventional probe station with minimal deviation, showing its pertinency towards PoC diagnosis of TBI. However, an extensive medical trial needs to be performed with TBI patients' samples for test kit validation, which we intend to take up shortly in collaboration with the ESIC Hospitals, Hyderabad.

#### Author contributions

Patta Supraja and Suryasnata Tripathy have defined the protocols, designed the experimental flow and prepared the manuscript. Patta Supraja has performed all the experimentation and interpreted the results. Dr. Shiv Govind Singh have conceived the problem statement.

#### Ethical Statement

This work has been approved by institutional ethical committee related to the ESIC Medical College & Hospital (Employees State Insurance Corporation: Sanathnagar, Hyderabad, India) and subjects gave informed consent to the work.

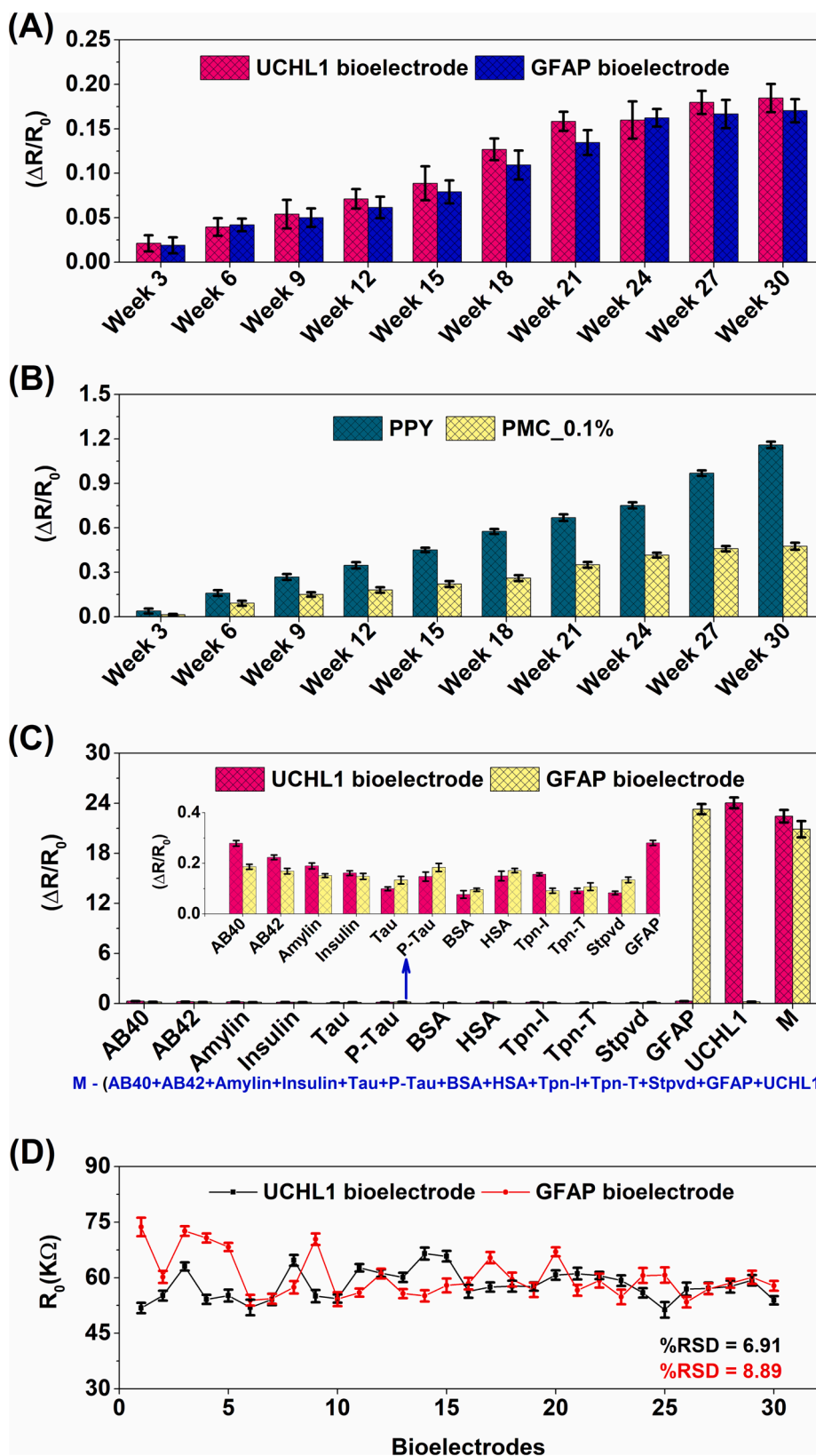


Fig. 5. (A) Stability of bioelectrodes - Relative normalized change in the resistance of PMC\_0.1 % nanocomposite-based UCHL1 and GFAP bioelectrodes over 30 weeks of storage duration (at 4 °C) with respect to day0; Responses of bioelectrodes measured every three weeks once (n = 3). (B) Stability of nanomaterials - Relative normalized change in the resistance of PPY and PMC\_0.1 % nanocomposite modified IDμEs over 30 weeks of storage duration with respect to Day0; Responses of nanomaterial modified electrodes measured every three weeks once (n = 3). (C) Selectivity/Interference analysis - Relative normalized change in resistance of UCHL1/GFAP bioelectrodes for 10 ng/mL concentration of specific and non-specific targets and a mixture of these compounds (M) (n = 3). (D) Absolute resistance ( $R_0$ ) change for reproducibility (n = 30) and repeatability (n = 4) analysis of UCHL1/GFAP bioelectrodes.

**Declaration of Competing Interest**

The authors declare that they have no known competing financial interests or personal relationships that could have appeared to influence the work reported in this paper.

**Data availability**

No data was used for the research described in the article.

## Acknowledgment

The authors acknowledge the Department of Science and Technology (Fund for Improvement of S&T infrastructure), Government of India for funding research. The authors also acknowledge Swati Mohanty who helped in designing the portable electronic readout platform.

## Appendix A. Supplementary material

Supplementary data to this article can be found online at <https://doi.org/10.1016/j.bioelechem.2023.108391>.

## References

- [1] P.K. Dash, J. Zhao, G. Hergenroeder, A.N. Moore, Biomarkers for the diagnosis, prognosis, and evaluation of treatment efficacy for traumatic brain injury, *Neurotherapeutics* 7 (2010) 100–114.
- [2] T. Ingebrigtsen, B. Romner, Biochemical serum markers of traumatic brain injury, *J. Trauma Acute Care Surg.* 52 (2002) 798–808.
- [3] S. Korfiatis, A. Papadimitriou, G. Stranjalis, C. Bakoula, G. Daskalakis, A. Antsaklis, D.E. Sakas, Serum biochemical markers of brain injury, *Mini Rev. Med. Chem.* 9 (2009) 227–234.
- [4] E. Kövesdi, J. Lückl, P. Bukovics, O. Farkas, J. Pál, E. Czeiter, D. Szellár, T. Dóczi, S. Komoly, A. Btki, Update on protein biomarkers in traumatic brain injury with emphasis on clinical use in adults and pediatrics, *Acta Neurochir. (Wien)* 152 (2010) 1–17.
- [5] J. Streeter, R.L. Hayes, K.K.W. Wang, Diagnostic protein biomarkers for severe, moderate and mild traumatic brain injury, in: *Sens. Technol. Glob. Heal. Mil. Med. Disaster Response, Environ. Monit. Biometric Technol. Hum. Identif. VIII, International Society for Optics and Photonics*, 2011: p. 80290N.
- [6] K. Samson, In the clinic-traumatic brain injury: FDA approves first blood test for brain bleeds after mild TBI/Concussion, *Neurol. Today.* 18 (2018) 12–18.
- [7] C. Tlili, L.N. Cella, N.V. Myung, V. Shetty, A. Mulchandani, Single-walled carbon nanotube chemoresistive label-free immunosensor for salivary stress biomarkers, *Analyst.* 135 (2010) 2637–2642.
- [8] M.A. Bangar, D.J. Shirale, W. Chen, N.V. Myung, A. Mulchandani, Single conducting polymer nanowire chemiresistive label-free immunosensor for cancer biomarker, *Anal. Chem.* 81 (2009) 2168–2175.
- [9] M.A. Bangar, D.J. Shirale, H.J. Purohit, W. Chen, N.V. Myung, A. Mulchandani, Single conducting polymer nanowire based sequence-specific, base-pair-length dependant label-free DNA sensor, *Electroanalysis.* 23 (2011) 371–379.
- [10] M. Durga Prakash, S.R.K. Vanjari, C.S. Sharma, S.G. Singh, Ultrasensitive, label free, chemiresistive nanobiosensor using multiwalled carbon nanotubes embedded electrospun SU-8 nanofibers, *Sensors.* 16 (2016) 1354.
- [11] B. Paul K, A.K. Panigrahi, V. Singh, S.G. Singh, A multi-walled carbon nanotube–zinc oxide nanofiber based flexible chemiresistive biosensor for malaria biomarker detection, *Analyst.* 142 (2017) 2128–2135. <https://doi.org/10.1039/C7AN00243B>.
- [12] S. Tripathy, A. Naithani, S.R.K. Vanjari, S.G. Singh, Electrospun polyaniline nanofiber based chemiresistive nanobiosensor platform for DNA hybridization detection, in: *2017 IEEE SENSORS, IEEE*, 2017: pp. 1–3.
- [13] S. Tripathy, V. Bhandari, P. Sharma, S.R.K. Vanjari, S.G. Singh, Chemiresistive DNA hybridization sensor with electrospun nanofibers: A method to minimize inter-device variability, *Biosens. Bioelectron.* 133 (2019) 24–31.
- [14] P. Supraja, S. Tripathy, R. Singh, V. Singh, G. Chaudhury, S.G. Singh, Towards point-of-care diagnosis of Alzheimer's disease: Multi-analyte based portable chemiresistive platform for simultaneous detection of  $\beta$ -amyloid (1–40) and (1–42) in plasma, *Biosens. Bioelectron.* 186 (2021), 113294.
- [15] M.R. Wiesner, G. V Lowry, P. Alvarez, D. Dionysiou, P. Biswas, Assessing the risks of manufactured nanomaterials, (2006).
- [16] P. Korshed, L. Li, D.-T. Ngo, T. Wang, Effect of storage conditions on the long-term stability of bactericidal effects for laser generated silver nanoparticles, *Nanomaterials.* 8 (2018) 218.
- [17] I. Chowdhury, M.C. Duch, N.D. Mansukhani, M.C. Hersam, D. Bouchard, Colloidal properties and stability of graphene oxide nanomaterials in the aquatic environment, *Environ. Sci. Technol.* 47 (2013) 6288–6296.
- [18] Y. Song, S. Ji, Y.-J. Song, R. Li, J. Ding, X. Shen, R. Wang, R. Xu, X. Gu, In situ redox microfluidic synthesis of core-shell nanoparticles and their long-term stability, *J. Phys. Chem. C.* 117 (2013) 17274–17284.
- [19] G. Casula, P. Cosseddu, Y. Busby, J.-J. Pireaux, M. Rosowski, B.T. Szczesna, K. Soliwoda, G. Celichowski, J. Grobelny, J. Novák, Air-stable, non-volatile resistive memory based on hybrid organic/inorganic nanocomposites, *Org. Electron.* 18 (2015) 17–23.
- [20] M. Spuch-Calvar, L. Rodriguez-Lorenzo, M.P. Morales, R.A. Alvarez-Puebla, L. M. Liz-Marzan, Bifunctional nanocomposites with long-term stability as SERS optical accumulators for ultrasensitive analysis, *J. Phys. Chem. C.* 113 (2009) 3373–3377.
- [21] K. Richter, A. Birkner, A. Mudring, Stabilizer-free metal nanoparticles and metal-metal oxide nanocomposites with long-term stability prepared by physical vapor deposition into ionic liquids, *Angew. Chemie Int. Ed.* 49 (2010) 2431–2435.
- [22] R.K. Goyal, *Nanomaterials and nanocomposites: synthesis, properties, characterization techniques, and applications*, CRC Press, 2017.
- [23] M. Govindhan, M. Amiri, A. Chen, Au nanoparticle/graphene nanocomposite as a platform for the sensitive detection of NADH in human urine, *Biosens. Bioelectron.* 66 (2015) 474–480.
- [24] Y. Wei, C. Gao, F.-L. Meng, H.-H. Li, L. Wang, J.-H. Liu, X.-J. Huang, SnO<sub>2</sub>/reduced graphene oxide nanocomposite for the simultaneous electrochemical detection of cadmium (II), lead (II), copper (II), and mercury (II): an interesting favorable mutual interference, *J. Phys. Chem. C.* 116 (2012) 1034–1041.
- [25] X. Cui, C.M. Li, J. Zang, S. Yu, Highly sensitive lactate biosensor by engineering chitosan/PVI-Os/CNT/LOD network nanocomposite, *Biosens. Bioelectron.* 22 (2007) 3288–3292.
- [26] N. Yang, X. Chen, T. Ren, P. Zhang, D. Yang, Carbon nanotube based biosensors, *Sensors Actuators B Chem.* 207 (2015) 690–715.
- [27] S. Xu, W. Yu, M. Jing, R. Huang, Q. Zhang, Q. Fu, Largely enhanced stretching sensitivity of polyurethane/carbon nanotube nanocomposites via incorporation of cellulose nanofiber, *J. Phys. Chem. C.* 121 (2017) 2108–2117.
- [28] P. Supraja, S. Tripathy, S.R.K. Vanjari, S.G. Singh, Label-free, ultrasensitive and rapid detection of FDA-approved TBI specific UCHL1 biomarker in plasma using MWCNT-PPY nanocomposite as bio-electrical transducer: A step closer to point-of-care diagnosis of TBI, *Biosens. Bioelectron.* 216 (2022), 114631.
- [29] H. Lampinen, P. Perala, O. Vainio, Novel successive-approximation algorithms, in: *2005 IEEE Int. Symp. Circuits Syst., IEEE*, 2005: pp. 188–191.
- [30] T. Ogawa, H. Kobayashi, M. Hotta, Y. Takahashi, H. San, N. Takai, SAR ADC algorithm with redundancy, in: *APCCAS 2008-2008 IEEE Asia Pacific Conf. Circuits Syst., IEEE*, 2008: pp. 268–271.
- [31] M. Farbod, S.K. Tadavani, A. Kiasat, Surface oxidation and effect of electric field on dispersion and colloids stability of multiwalled carbon nanotubes, *Colloids Surfaces A Physicochem. Eng. Asp.* 384 (2011) 685–690.
- [32] P. Nie, C. Min, H.-J. Song, X. Chen, Z. Zhang, K. Zhao, Preparation and tribological properties of polyimide/carboxyl-functionalized multi-walled carbon nanotube nanocomposite films under seawater lubrication, *Tribol. Lett.* 58 (2015) 1–12.
- [33] J.V. Rojas, M. Toro-Gonzalez, M.C. Molina-Higgins, C.E. Castano, Facile radiolytic synthesis of ruthenium nanoparticles on graphene oxide and carbon nanotubes, *Mater. Sci. Eng. B.* 205 (2016) 28–35.
- [34] K. Ahmed, F. Kanwal, S.M. Ramay, S. Atiq, R. Rehman, S.M. Ali, N.S. Alzayed, Synthesis and characterization of BaTiO<sub>3</sub>/polypyrrole composites with exceptional dielectric behaviour, *Polymers (Basel).* 10 (2018) 1273.
- [35] M.G. Smitha, M.V. Murugendrapa, Effect of barium lanthanum manganite nano particle on the electric transport properties of polypyrrole at room temperature, *J. Mater. Sci. Mater. Electron.* 30 (2019) 10776–10791.
- [36] H. Vijeth, S.P.A. Kumar, L. Yesappa, M. Niranjana, M. Vandana, H. Devendrapa, Influence of nickel oxide nanoparticle on the structural, electrical and dielectric properties of polypyrrole nanocomposite, in: *AIP Conf. Proc., AIP Publishing LLC*, 2019: p. 150029.
- [37] B. Zhang, Y. Xu, Y. Zheng, L. Dai, M. Zhang, J. Yang, Y. Chen, X. Chen, J. Zhou, A facile synthesis of polypyrrole/carbon nanotube composites with ultrathin, uniform and thickness-tunable polypyrrole shells, *Nanoscale Res. Lett.* 6 (2011) 1–9.
- [38] S.G. Bachhav, D.R. Patil, Study of polypyrrole-coated MWCNT nanocomposites for ammonia sensing at room temperature, *J. Mater. Sci. Chem. Eng.* 3 (2015) 30.
- [39] M.A. Rashed, M. Faisal, M. Alsaifi, S.A. Alsaifi, F.A. Harraz, MWCNT-Doped Polypyrrole-Carbon Black Modified Glassy Carbon Electrode for Efficient Electrochemical Sensing of Nitrite Ions, *Electrocatalysis.* 12 (2021) 650–666.
- [40] S. Rafique, R. Sharif, I. Rashid, S. Ghani, Facile fabrication of novel silver-polypyrrole-multiwall carbon nanotubes nanocomposite for replacement of platinum in dye-sensitized solar cell, *AIP Adv.* 6 (2016) 85018.
- [41] S. Tripathi, Y.V. Kumar, A. Agrawal, A. Prabhakar, S.S. Joshi, Microdevice for plasma separation from whole human blood using bio-physical and geometrical effects, *Sci. Rep.* 6 (2016) 1–15.
- [42] D.R. Thévenot, K. Toth, R.A. Durst, G.S. Wilson, Electrochemical biosensors: recommended definitions and classification, *International Union of Pure and Applied Chemistry: Physical Chemistry Division, Commission 1.7 (Biophysical Chemistry); Analytical Chemistry Division, Commission V.5 (Electroanalytical, Biosens. Bioelectron.* 16 (2001) 121–131. [https://doi.org/https://doi.org/10.1016/S0956-5663\(01\)00115-4](https://doi.org/https://doi.org/10.1016/S0956-5663(01)00115-4).